Extraction and Visualization of Poincaré Map Topology for Spacecraft Trajectory Planning

Category: Application

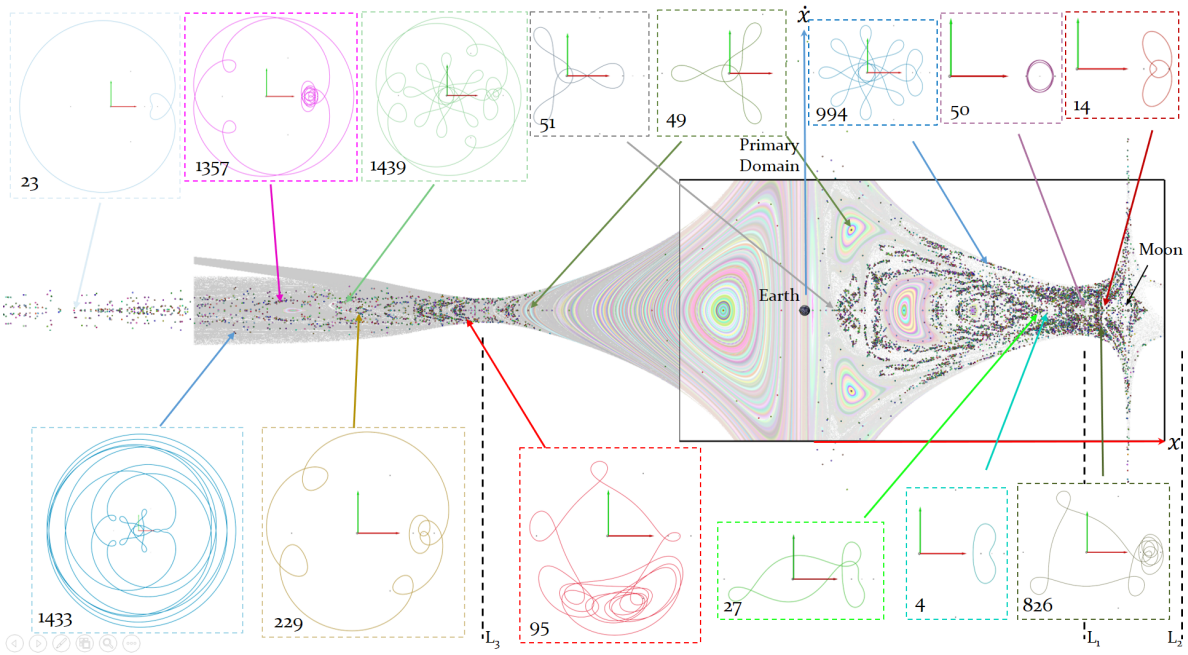

Fig. 1. Fixed points in the Earth-Moon system at $C = 2.96$. This is the collective result for the trials in Table 2.

Abstract—*Astrodynamics*, the application of celestial mechanics to predict the motion of space vehicles, incorporates many dynamical models where analysis and design is assisted with Poincaré maps. Planning a low-cost spacecraft trajectory that satisfies mission constraints often involves selecting a suitable path through the interconnected web of Poincaré map structures such as fixed points (or periodic orbits) and invariant manifolds present in multi-body gravitational systems. This paper considers the visualization and interactive exploration of this topology to assist spacecraft trajectory planning. We propose new algorithmic solutions that address the specific challenges posed by the extraction of the topology in astrodynamics problems. The resulting computational framework is then applied to the circular restricted three-body problem (CR3BP) where it reveals novel periodic orbits with the relevant invariant manifolds in a suitable format for interactive manifold arc selection. Two representative design cases demonstrate how spacecraft path planners can fully exploit the natural dynamics pathways resulting from the proposed method for low-control effort designs.

Index Terms—Astrodynamics, trajectory planning and design, Poincaré map, dynamical systems, topology extraction, invariant manifolds, chaos.

1 Introduction

Space missions collect scientific data about celestial bodies and astronomical phenomena, yielding new knowledge and insight about the origins of the universe. The design of a spacecraft trajectory is the key to success of any mission. The spacecraft path must deliver the scientific objectives under the constraints imposed by the laws of physics and a targeted mission price. Although many factors influence the mission cost, the price is strongly driven by the spacecraft mass [24], which is represented by three fundamental components – payload, support structure, and propellant. The payload is the collection of science instruments required to deliver the mission data whereas the support structure consists of the spacecraft operational equipment (e.g., bus, antenna, engines, propellant tanks, solar arrays, etc). Course corrections or maneuvers are accomplished by performing a change in spacecraft velocity (or ΔV) while expelling propellant. Although propellant is necessary to perform maneuvers, less propellant mass is typically preferred in favor of more payload mass. Such a trade-off produces more scientific return for the mission while potentially reducing the overall monetary cost. In this context, the role of a spacecraft trajectory designer is to devise a pathway that minimizes the amount of propellant required to transport the vehicle to mission objectives.

Leveraging chaotic dynamics available in multi-body gravitational models permits small maneuvers to impart large alterations in downstream spacecraft destinations. Thus, spacecraft trajectory designers exploit naturally existing dynamics in such nonlinear multi-body models as ideal transfer options to minimize propellant usage. Unfortunately, pinpointing favorable maneuver locations in position-space visualizations is quite difficult since orbital structures repeatedly overlap and information about velocity magnitudes is limited due to the high-dimensional nature of the problem. As an alternative, pertinent dynamical flow is observed from a global perspective via a surface of section utilizing the Poincaré map (or first-return mapping). The resulting Poincaré section preserves a phase-space snapshot of all behavior that crosses a given hyperplane defining the surface of section. The problem dimensionality is then reduced into a tractable arena (2D or

3D) while also highlighting velocity differentials. Existing Poincaré map topology extraction methods [21, 15] exploit local linear models to extract topological structures embedded in nonlinear dynamics. Knowing the topological skeleton that reflects how orbital structures connect freely or with small ΔVs supplies spacecraft path-planning with a plethora of novel options and pathways that save on propellant usage (typically at the expense of extended flight time).

Yet, the automatic extraction of Poincaré map topology within multi-body gravitational models remains challenging due to numerical sensitivities during path simulation and violated assumptions in the Poincaré map. This paper presents significant technical contributions to Poincaré map topology extraction that address the specific numerical and structural challenges raised by multi-body gravitational systems. Adaptive computation techniques are applied for enhanced characterization of behavior and the detection of periodic orbits. A similar adaptive strategy is employed for the development of invariant manifolds, resulting in a tree-like data structure that simplifies invariant manifold interaction during a design process.

Precise knowledge of the Poincare map topology provides a detailed structure for planning spacecraft trajectories. Natural transfers between periodic orbits residing within chaotic flow spaces exist and are often exploited for transfer designs with minimal maneuver costs [13, 11, 22, 8]. Most of the structure available from previous work, however, relies heavily on the known periodic orbits of multi-body dynamics. The fixed point extraction solution described in this paper uncovers a wealth of previously unknown periodic orbits that open transfer design possibilities. In addition, our invariant manifold generation technique allows us to interactively identify robust and accurate navigation pathways across chaotic regions, which in turn, enables the rapid definition of free-flowing connections between any two arbitrary unstable orbits. Over all, the proposed visual computing framework greatly expands the design space for mission development and can lead to design previously unknown to astrodynamicists.

2 Circular Restricted Three-Body Problem

The gravitational model considered in this paper pertains to the motion of a spacecraft (or other exceptionally small body) under the influence of two celestial bodies that form an orbital system (*e.g.*, Earth and Moon, Sun and Earth, or Saturn and Titan). The motion of a spacecraft under the influence of the combined gravitational field is then simplified to the area-preserving circular restricted three-body problem (CR3BP) model. Assume a pair of gravitating bodies (P_1 and P_2 with corresponding masses $m_1 > m_2$) move about their common barycenter in circular orbits; spacecraft flight is then simulated with the CR3BP equations of motion such that the path evolves only in 2D. Let the gravity parameter, μ, represents a ratio of masses: $\mu = m_2/(m_1+m_2)$. The state vector $\boldsymbol{x} = [x, y, \dot{x}, \dot{y}]^T$ (with $\dot{a}$ denoting the time derivative $\frac{da}{dt}$) relates the position and velocity of a small body ($m << m_1, m_2$) with respect to the barycenter. Coordinates are expressed in a rotating reference frame with the origin at the barycenter, the axis $\hat{\boldsymbol{x}}$ aligned with the $\overrightarrow{P_1P_2}$ line and $\hat{\boldsymbol{y}}$ points concurrent to the velocity vector of P_2 with respect to P_1. If we express the planar position (x, y) and velocity $(\dot{x}, \dot{y})$ coordinates in nondimensional units [3][1] then a pseudo-potential value (Υ) is realized as a function of only position such that

$$\Upsilon(x,y) = \frac{1-\mu}{r_1} + \frac{\mu}{r_2} + \frac{1}{2}(x^2+y^2), \tag{1}$$

for planar motion. Here, r_1 (resp. r_2) denotes the distance from the spacecraft to P_1 (resp. P_2). The CR3BP model is then evaluated as the second-order system described by

$$\ddot{x} - 2\dot{y} = \frac{\partial \Upsilon}{\partial x} \text{ and } \ddot{y} + 2\dot{x} = \frac{\partial \Upsilon}{\partial y}, \tag{2}$$

which defines an ODE on the state vector $\boldsymbol{x}$. Note, a third out-of-plane (or z) component of flow also exists but is decoupled from planar motion [19, 3]. The Hamiltonian in the CR3BP model is the Jacobi constant C following

$$C = 2\Upsilon(x,y) - (\dot{x}^2 + \dot{y}^2), \tag{3}$$

with the total planar velocity $V = (\dot{x}^2+\dot{y}^2)^{\frac{1}{2}}$ [19, 3]. The constancy of C implies that the system is time-invariant and area-preserving [10]. C is an orbital energy term that is invariant under the action of the CR3BP but can be modified during maneuvers. Note that larger C values correspond to a lower energy level.

Some periodic orbits of the CR3BP play a central role for mission design. The four *Lagrange points* are locations where the gravitational forces of both bodies are equal. *Lyapunov orbits* are planar orbits about the Lagrange points. *Resonant orbits* have an integer period ratio with respect to the Moon's orbital period about the Earth (*e.g.*, 4:1, 3:4, 2:1). The *Distant Retrograde Orbit (DRO)* circles the smaller body (*e.g.*, Moon) in a clockwise direction. *Gateways* are areas of space near the Lagrange points where transition between areas is first possible. The term *capture* refers to the access of an orbit about a celestial body. A *ballistic capture* occurs when capture is enabled by gravity and does not require a maneuver.

3 Topological Structure in Poincaré Maps

We briefly review in this section basic theoretical notions related to area preserving maps and Poincaré maps that pertain to the CR3BP. Additional details are given in prior work on map visualization [21, 15] and in classical references [7, 10].

A dynamical system associated with a vector field $\boldsymbol{v}$ defines a *flow map* $\boldsymbol{x}_f$ with $\dot{\boldsymbol{x}}_f = \boldsymbol{v}(\boldsymbol{x}_f)$ such that $\boldsymbol{x}_f(t, t_0, \boldsymbol{x_0})$ describes the transport from an initial state $\boldsymbol{x}_0$ at t_0 to its later state at time t.

Let Σ represent a hyperplane that is transverse[2] to the flow and let $\boldsymbol{x}_0$ be an initial state on Σ. The Poincaré map, or the first-return map $P(\boldsymbol{x}_0) := \boldsymbol{x}_0 \mapsto P_\Sigma(\boldsymbol{x}_0)$ corresponds to the first crossing of Σ by the trajectory starting at $\boldsymbol{x}_0$. Multiple iterates of the Poincaré map are then computed by compounding the first return map, *e.g.*, $P^p(\boldsymbol{x}_0) = P_\Sigma(P_\Sigma(\ldots P_\Sigma(\boldsymbol{x}_0)))$ for p returns. Both the initial state and first return to Σ are shown on the green hyperplane in Fig. 2(a).

Three dynamic behaviors co-exist on a Poincaré map for a so-called *near-integrable* system like the planar CR3BP: *periodicity*, *quasi-periodicity*, and *chaos*. Visible in Fig. 2(a), a periodic state, $\boldsymbol{x}^*$, returns to the same state through the Poincaré map, *i.e.,* $P^p(\boldsymbol{x}^*) = \boldsymbol{x}^*$, where p represents the number of returns required for a p-periodic trajectory to complete an orbit. These p distinct returns are called *fixed points* of the Poincaré map and can be either *centers* or *saddles*. Refer to Fig. 2(b). So-called *stable* and *unstable manifolds* emerge from the saddle points indicating dynamical flow into and out of the periodic orbits, respectively. A fundamental feature of Poincaré map topology is the connection between saddle points in which stable and unstable manifolds intersect an infinite number of times, creating chaotic tangles as seen in Fig. 2(b).

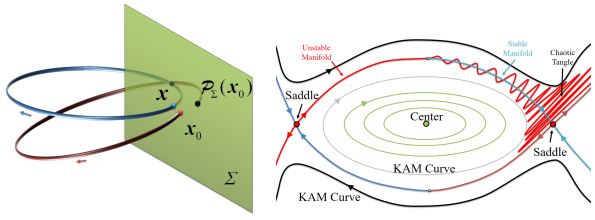

(a) A Poincaré map (b) Poincaré map topology

Fig. 2. Available topological structure associated with a Poincaré map in a near-integrable dynamical system [21, 7, 10].

For integrable and near-integrable Hamiltonian systems with two-degrees of freedom, it can be shown that the dynamics is confined

[1] For reference, a nondimensional position unit in the Earth-Moon (*EM*) system is equivalent to 384388.174 km whereas a nondimensional velocity unit is 1.02456261 km/s.

[2] The plane is transverse if the vector field is nowhere tangent to Σ

to a torus, in which the motion is then characterized by the so-called *winding number* $w = \frac{\omega_1}{\omega_2}$, where ω_1 and ω_2 are the poloidal and toroidal rotation frequencies, respectively. The winding number permits to classify trajectories: rational numbers $w = \frac{q}{p}, p, q \in \mathbb{N}^*$, p and q mutually prime correspond to periodic orbits. In this case q corresponds to the number of poloidal rotations performed during p toroidal rotations and p is the period of the fixed point. In contrast, quasi-periodic trajectories possess irrational winding number: a quasi-periodic orbit will never trace exactly the same path along the torus, and in the case of chaotic trajectories, the winding number is undefined.

The state transition matrix (STM) $\Phi(t,t_0)$ evaluated from an initial time t_0 to a later time t is defined as the spatial derivative of the flow map $\boldsymbol{x}_f$ with respect to its initial condition. Note that $\Phi(t,t_0)$ can be computed concurrently with the integration the planar CR3BP model (Eq. (2)) using the spatial derivative of the vector field $\boldsymbol{v}$. In the vicinity of periodic orbits, the full-period STM matrix $\mathscr{M} = \Phi(T,0)$, called the *monodromy* matrix, offers a linearized description of the local dynamics and provides the information needed to determine the invariant subspaces associated with stable and unstable manifolds. The type of a fixed point is determined by the eigenvalues of $\mathscr{M}$. The eigenspaces of the fixed point (E^i with $i = S,C,U$ for stable, center, and unstable, respectively) indicate the tangent of the global manifolds W^i at the fixed point location. Because the determinant of the monodromy matrix in an area preserving map is one, its eigenvalues must exist as reciprocal pairs. The eigenvalues determine the eigenspace type via

$$E^S \in \|\lambda_i\| < 1, E^C \in \|\lambda_i\| = 1, E^U \in \|\lambda_i\| > 1. \tag{4}$$

An alternative stability classification is possible through a stability index, ν_{SI}, defined as

$$\nu_{SI} = \tfrac{1}{2}(\mathrm{tr}(\mathscr{M}) - 2). \tag{5}$$

Orbits are unstable when $|\nu_{SI}| > 1.0$ and stable otherwise.

4 Prior Work on Poincaré Map Topology

Our proposed solution for the visual analysis of the CR3BP topology leverages prior work on Poincaré map topology visualization [21] and its recent extension to multi-body gravitational environments [15]. We summarize here the main steps of the method. The next section discusses the algorithmic improvements that we performed to enable the visual analysis presented in Section 6.

Poincaré map sampling. First, a regular sampling of the Poincaré map is performed. The numerical integration is carried out for a fairly large number of toroidal revolutions and all the intermediate returns to the Poincaré section are recorded for the next phase.

Trajectory classification. Next, the winding number associated with each computed trajectory is computed. A best rational approximation of this number $w = \frac{q}{p}$ is then determined such that the denominator $p \in \mathbb{N}$ does not exceed a user-defined maximum period p_{max} for the analysis. For the CR3BP , Schlei *et al.* [15] consider three distinct winding numbers computed directly in the standard rotating coordinates of the problem: $\mathbf{W} = \left(w_{x\dot{x}}, w_{x\dot{y}}, w_{\dot{x}\dot{y}}\right)$, which affords a refined characterization of the dynamics.

Cell-wise index computation. The winding numbers computed previously allow the algorithm to consider only a small number of periods in the analysis of individual sampling cells. In each cell the Poincaré index of the vector-valued (displacement) mapping

$$\boldsymbol{\Delta} = P^p(\boldsymbol{x}) - \boldsymbol{x}. \tag{6}$$

is computed via adaptive sampling along the edges of the cell for each relevant period. If the sampling resolution was chosen fine enough in the first step, the resulting index values are expected to be either -1 (saddle point in the cell), $+1$ (center present), or 0 (no fixed point).

Fixed point extraction. If a non-zero index has been computed, a fixed point search is performed in the cell at the corresponding period. A fixed point corresponds to a zero value of the displacement map $\boldsymbol{\Delta}$ and a Newton iterative method is used to determine the corresponding location. A multiple shooting method is used to improve the numerical convergence in the CR3BP [15].

Manifold extraction. Once the location of a fixed point of P^p has been resolved with sufficient accuracy the linear type of the fixed point (center or saddle) is determined through eigenanalysis of the monodromy matrix. If the eigenvalues correspond to a saddle type (see Eq. (4)), the corresponding invariant manifolds are then constructed through a succession of shooting problems [5] and their progression stops when they approach another saddle-type fixed point.

5 Robust and Efficient Poincaré Map Topology Extraction in the CR3BP

While prior work [15] offers a general framework for Poincaré map topology extraction in the CR3BP, it suffers from a number of significant limitations that make it unsuitable for our visual analysis objectives. Algorithmic and numerical solutions are discussed here that were implemented to address these shortcomings.

5.1 Adaptive Poincaré map sampling

To permit a reliable detection of potential fixed points, the Poincaré index of the displacement map $\boldsymbol{\Delta}$ (Eq. (6)) must be evaluated around areas of the map that are small enough to contain at most a single fixed point for the considered period [18]. Hence, a very high resolution sampling yielding tiny cells is typically desirable. However, this approach is computationally prohibitive and a more subtle data-driven sampling is needed.

We first observe that the winding number is a locally smoothly varying characteristic parameter, within regions of regular dynamics. Therefore, the variance in the winding number set $\boldsymbol{W}$ can be utilized to determine when to subdivide a cell. Ideally, a cell that isolates fixed points should not exhibit significant variations in its associated $\boldsymbol{W}$ values. Practically we adopt an adaptive refinement strategy for the Poincaré map sampling that uses two quality measures to enforce this property.

First, we impose an upper bound on the range of winding values present in a cell, *i.e.,*

$$\Delta \boldsymbol{W}_c = \boldsymbol{W}_{max \forall v} - \boldsymbol{W}_{min \forall v} \leq \boldsymbol{\psi}_w, \tag{7}$$

where $v \in [1,4]$ designates the cell vertices, and $\boldsymbol{\psi}_w$ is a user-defined parameter. The values of $\boldsymbol{\psi}_w$ bound the dynamic range within a cell, so smaller values yield smaller analysis cells during the subdivision process. Our second control measure aims to ascertain the local quasi-linearity of the winding numbers variations. If $\boldsymbol{W}_i$ represents a winding number set for a Poincaré section point (with index i) inside a particular analysis cell, then all n internal points to a cell should satisfy

$$\boldsymbol{W}_{min \forall c} - \boldsymbol{\varepsilon}_w \odot \boldsymbol{\psi}_w \leq \boldsymbol{W}_i \leq \boldsymbol{W}_{max \forall c} + \boldsymbol{\varepsilon}_w \odot \boldsymbol{\psi}_w. \tag{8}$$

$\boldsymbol{\varepsilon}_w$ is another set of user-specified parameters, and the $\odot$ symbol represents element-by-element multiplication of vectors ($\boldsymbol{a} \odot \boldsymbol{b} = (a_1 b_1, a_2 b_2, a_3 b_3)$). Any cell that fails the criteria in either Equation 7 or Equation 8 encompasses too much dynamical behavior or surrounds a spatially diverse dynamical region, and is marked for subdivision.

Practically, we use a multiresolution mesh data structure that records winding numbers both at the sampling vertices and inside the cells. Since all Poincaré section crossings of a given trajectory share the same winding numbers set $\boldsymbol{W}$ as the initial vertex, each one of the $p-1$ returns, or $P^q(\boldsymbol{x})$, $q \in [1, p-1]$, is assigned the same $\boldsymbol{W}$ values. These values are added to the cell containing the return and are then tested as part of the subdivision criteria in Eq. (8). When required, cells are regularly subdivided with internal data assigned to the corresponding quadrant within the original cell. A user-specified maximum depth level parameter, d_{max}, is employed to represent the total number of subdivision layers allowed. Cells are also subdivided if any corner has an undefined winding number.

Fig. 3 shows the adaptive resolution mesh produced in the domain D_{EM} for a maximum refinement depth $d = 3$. The initial grid is shown

in thick gray lines. The highest resolution is achieved in chaotic regions where the dynamics is most complex. This result is in fact excellent from an astrodynamics perspective since the saddles embedded in chaos offer the most versatile transfer opportunities. Regions of regular dynamics, in contrast, are coarsely resolved, as expected.

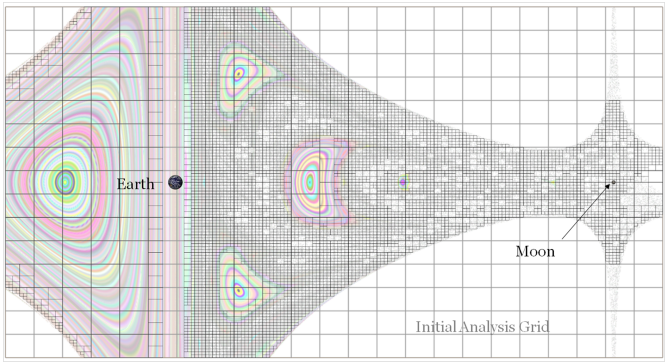

Fig. 3. Adaptive cell subdivision based on the winding number set $\boldsymbol{W}$ applied to the domain D_{EM} with parameters $C = 2.96$ and $d_{max} = 3$.

5.2 Poincaré section transversality

An issue that frequently prevents the computation of the Poincaré index in existing techniques is the presence of discontinuity of the $\boldsymbol{\Delta}$ mapping along cell edges. Two properties of the CR3BP can explain this behavior: highly sensitive dynamics and transversality violation of the flow map for the chosen section Σ.

Transversality violations are typically the result of one of two specific trajectory events. First, trajectories that are tangent to the section along their path generate discontinuities in $\boldsymbol{\Delta}$, see Fig. 5.2. A second event is an exact intersection by the trajectory of a singularity in the model such as the primaries in CR3BP (exemplified in Fig. 5.2).

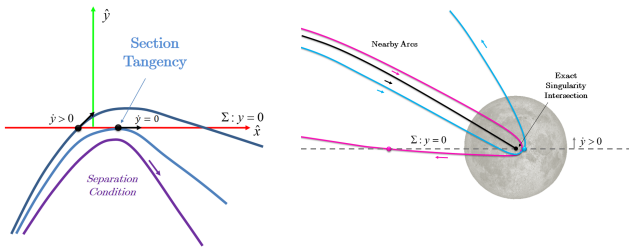

Fig. 4. Transversality violation types in the CR3BP. Left: section tangency, Right: singularity intersection.

5.3 Resolving the Poincaré Index

We perform the evaluation of the Poincaré index in non-transverse cells by considering the behavior of $\boldsymbol{\Delta}$ in the limit approaching a transversality violation. A discontinuity of $\boldsymbol{\Delta}$ at some location $\boldsymbol{g}$ on the closed curve Γ for period p creates a discontinuity in the Poincaré index at $\boldsymbol{g}$. However, since the limits of the angular coordinate $\alpha(\boldsymbol{\Delta}(\boldsymbol{g}))$ exist in various directions approaching $\boldsymbol{g}$, the Poincaré index can be expressed as the summation of improper integrals

$$\kappa = \frac{1}{2\pi}\oint_{\Gamma} d\alpha(\boldsymbol{\Delta}) = \frac{1}{2\pi}\left(\int_{\boldsymbol{\gamma}_0}^{\boldsymbol{g}} d\alpha(\boldsymbol{\Delta}) + \int_{\boldsymbol{g}}^{\boldsymbol{\gamma}_0} d\alpha(\boldsymbol{\Delta})\right), \qquad (9)$$

where $\boldsymbol{\gamma}_0$ is a starting point along Γ ($\boldsymbol{\gamma}_0 \neq \boldsymbol{g}$).

The adaptive edge sampling approach already used in prior work [15] is augmented with additional heuristics to detect transversality violations. Subsequent map states along cell edges are tested for transversality violations via a set of heuristic trials that search for fundamental differences in map information. The adaptive subdivision of an edge localizes the locations of $\boldsymbol{g}$ and generates sufficient approximations of the limiting values of $\alpha(\boldsymbol{\Delta}(\boldsymbol{g}))$. Luckily, all information required for heuristic detection is available during numerical simulation or easily retrieved from the output. It should be noted that transversality violations tend to form coherent contours on the section domain that represent fundamental transitions between trajectory types. This allows us to heuristically detect the two types of transversality violations and resolve the Poincaré index using a piecewise integral.

5.4 Fixed Point Refinement

The single shooting and multiple shooting solutions used previously to find fixed points are only moderately successful for our needs because each differential corrections technique possesses varying convergence properties and will often fail to find a fixed point. To remedy this situation, we apply differential corrections procedures in a predefined sequence chosen to maximize the convergence basin of the fixed point [14]. Starting with single shooting refinement, we switch to the variable-time multiple shooting method if this first attempt fails. If both solutions fail, we apply a quasi-Newton single shooting method, which is significantly more computationally expensive than the previous two but possesses stronger convergence properties.

5.5 Initial Guess for Fixed Points

Irrespective of the chosen refinement procedure, the refinement result is still heavily contingent on the quality of the initial guess. Our solution starts by sampling $\boldsymbol{\Delta}$ at a set of regularly distributed positions within the cell. Instead of working directly with $\boldsymbol{\Delta}$, however, we consider the map tangent $\boldsymbol{\eta}(\boldsymbol{x})$, defined as $\boldsymbol{\eta}(\boldsymbol{x}) = P^{p}(\boldsymbol{x}) - P^{-p}(\boldsymbol{x})$, which can be seen as a low-pass filtering that cancels out the dominance of the unstable mode in the vicinity of a saddle-type[3] fixed point [18, 10]. Practically, if the considered variable is $\boldsymbol{\zeta} = \boldsymbol{x} - \boldsymbol{s}$ with $\boldsymbol{s}$ representing the saddle-type fixed point location, then a quadratic model of the sampled dynamic is formed as

$$\dot{\boldsymbol{\zeta}} = A_s\boldsymbol{\zeta} + \tfrac{1}{2}\boldsymbol{\zeta}^T\underline{Q}\boldsymbol{\zeta}. \qquad (10)$$

Note, A_s is a 2×2 matrix, and $\underline{Q}$ is a $2\times 2\times 2$ tensor where $\underline{Q} = 0$ in the linear model. A Levenberg-Marquardt optimization process is applied to fit the model to the sampled data [12] and infer the approximate location of the fixed point.

Unfortunately, the model-fitting strategy outlined above cannot be applied in cells containing transversality violations. In such cases we apply a different approach, namely we identify the position along each edge of the cell where the norm $|\boldsymbol{\Delta}|$ is minimal and then sample this same quantity along the 6 possible lines that connect these 4 minima, seeking the minimal norm inside the cell since one these lines should closely match the stable manifold of a saddle-type fixed point.

5.6 Invariant Manifold Extraction

Eigenanalysis of the monodromy matrix $\mathscr{M}$ allows us to determine the stability type (saddle or center) of each discovered fixed point (Equation 4). If a saddle type is identified, the construction of the invariant (stable and unstable) manifolds constitutes the last step of the topology extraction and we derive eigenvectors and stability index (Equation 5) from $\mathscr{M}$.

Prior work [21, 15] directly applied to the construction of invariant manifolds a method proposed by England *et al.* [5], which proceeds through a series of two-point boundary problems that aim to ensure smoothness and fine sampling of the manifold. Unfortunately, this solution does not handle the issue raised by transversality violations in the CR3BP, nor does it provide any guidance to accommodate the numerical challenges associated with this particular system. We describe in the following our improvements of this method.

Manifold Extraction with Curve-Refinement. Consider two adjacent positions $\boldsymbol{\phi}_i$ and $\boldsymbol{\phi}_{i+1}$ that form a segment $w = \overline{\boldsymbol{\phi}_i\boldsymbol{\phi}_{i+1}}$ on the manifold. We further assume that both positions are close enough

[3] Saddles are far more challenging to extract than centers and much more likely to explain situations of failed convergence

such that linear interpolation between these two positions yields positions that are themselves on the manifold. Applying the Poincaré map P^p to any such intermediate position will result in a new position further downstream on the manifold. Refer to Fig. 5 (top). The basic

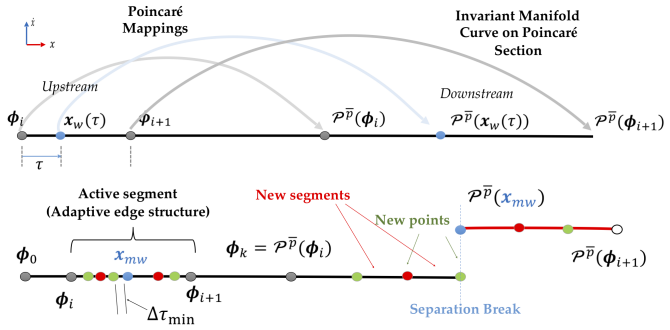

Fig. 5. Top: Schematic of a 1D invariant manifold curve on the Poincaré section. Bottom: Generating new downstream manifold points and segments through a transversality violation.

idea of the algorithm by England *et al.* [5] is that adaptive sampling of the segment w by the Poincaré map, controlled by curve quality checks, allows one to construct the next segment $= \overline{\boldsymbol{\phi}_{i+1}\boldsymbol{\phi}_{i+2}}$ on the manifold and ultimately extract the entire manifold by repeating this operation, see Fig. 5. Our solution follows the same approach while simultaneously checking for Poincaré map discontinuities along the way, thereby explicitly handling transversality violations.

The heuristics for detecting transversality violations during Poincaré index evaluation are reapplied alongside the curve-refinement criteria. If a downstream transversality violation is detected between consecutive segment samples, the segment is bisected on that interval. Subdivision continues until the distance between consecutive points reaches a user-prescribed minimal distance ($u_{\min}$, which corresponds to a relative distance $\Delta\tau_{\min}$). An example is depicted in Fig. 5 (bottom) where downstream mappings are color-coded by their initial position on the active segment: a downstream transversality violation exists between $\boldsymbol{\phi}_i$ and the midpoint $\boldsymbol{x}_{mw}$, and subdivision localizes the separation condition when the parameter differential is below $\Delta\tau_{\min}$.

Stopping Criteria. Recent work has shown that manifolds encounter other saddle points in the same island chain, a case that is prevalent in the CR3BP. Practically, we found two criteria primarily effective in controlling the useful downstream length of an invariant manifold on the Poincaré section.

The first stopping criteria tracks a practical measure for spacecraft trajectory planning. We saw previously that the manifold construction algorithm essentially maps upstream segments to downstream segments, thereby creating a parent-child relationship between them. Our algorithm caps the manifold progression by stopping when the depth of this relationship reaches a maximum depth $d_{w,\max} = 5$ (or $P^{5\overline{p}}(\boldsymbol{x})$).

The second stopping condition observes simultaneous advection of manifolds from the same periodic orbit for the detection of saddle-loops. Newly-generated downstream segments from both the stable and unstable manifolds of the *same periodic orbit* are compared in position and direction to detect if the segments overlap, indicating a KAM torus[10, 14].

Screening Computations Given the high computational cost of manifold construction, we perform several tests beforehand to prevent unnecessary computations.

First, we pre-screen for potentially impractical structures for spaceflight, *i.e.,* periodic orbits with exceptionally high instabilities. A threshold cutoff is established on stability index magnitude at $|\nu_{SI}| > 10^6$ (refer to Equation 5). In addition, more screening (or a lower $|\nu_{SI}|$ cutoff) reduces the overall workload required by our method and is often implemented in practice. Suggested thresholds are listed in Table 1.

A second important observation is that a lower bound is necessary for $u_{\min}$ (which regulates upstream manifold segment subdivisions) as a transfer stipulation for realistic spaceflight. Error in real-world devices such as sensors and engines translate into limitations on state acquisition and deliverable maneuvers; if a particular transfer requires that the position and velocity match a desired state to 10^{-6} m and 10^{-6} m/s, for example, that trajectory may not be flight worthy as many instruments cannot deliver that level of accuracy [23, 6]. Spacecraft state determination outside of low Earth orbits is limited to an accuracy of 3 km for position and 0.1 mm/s for velocity based on measurement error of standard capabilities [26]. Practically, we require $u_{\min}$ values above 2×10^{-5} (nondimensional map displacement) for the Earth-Moon system, which is equivalent to 2.05 cm/s for velocity and 7.69 km for position. Note that the value of $u_{\min}$ is different across CR3BP systems. Refer to Table 1 for suggested values.

System	$u_{\min}$	$\Delta_{\min}$	$\Delta_{\max}$	$\alpha_{\max}$	$(\Delta\alpha)_{\max}$	$\lvert\nu_{SI}\rvert_{\max}$
EM	2×10^{-5}	1×10^{-5}	0.1	0.3 (17.2°)	0.001	2.5×10^{3}
ST	4×10^{-6}	1×10^{-6}	0.05	0.1 (5.7°)	0.001	2.5×10^{3}
SEnc	1×10^{-6}	1×10^{-6}	0.05	0.1 (5.7°)	0.001	5.0×10^{3}

Table 1. Heuristic parameters employed for invariant manifold advection in the indicated CR3BP systems. Phase space displacement values are listed in nondimensional units (as defined by England *et al.*[5]).

Manifold Arc Extraction Implementing manifolds within trajectory design applications requires the ability to select an invariant manifold state from the Poincaré map visualization and reconstitute the arc. Simply propagating a user-selected invariant manifold state upstream (i.e., forward-time for W^S and reverse-time for W^U) often fails because of the flow-dividing nature of the invariant manifolds. Both W^S and W^U represent a ridge separating local nonlinear upstream flow behavior. Such a ridge can be 'sharp,' i.e., analogous to the summits of a mountain range; a slight deviation off the ridge produces a rapid departure from the invariant manifold curve during an upstream propagation, similar to sliding down the mountain side [9].

Upstream manifold arc reconstruction with our method circumvents the challenges associated with propagating manifold arcs upstream with a very effective data structure format resulting from the manifold advection procedure. Our manifold extraction process advects states sampled from an upstream manifold segment to create a new group of downstream segments through the Poincaré map; such a transaction inherently links invariant manifold segments via the Poincaré map and organically forms segment data into a *manifold segment tree*. To illustrate, sample manifold segments near the origin location of the advection procedure are arranged as a staircase schematic indicating depth levels (d_w) as in Fig. 6; each step down symbolizes the downstream progression to the next group of segments after $\overline{p}$ map iterates. To reconstruct the entire upstream trajectory from the fixed point, the

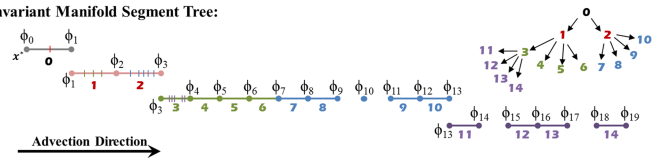

Fig. 6. As the invariant manifolds are progressed via curve-refinement, the spawning of new manifold segments generates a tree structure that can be employed for accessing data.

downstream mappings supply a reliable numerical simulation framework to return the intermediate trajectory states between the parent and child manifold segments as such downstream simulations are employed during the construction of the 1D invariant manifold curves. The complete upstream arc is reconstructed by numerically simulating each upstream node to the subsequent downstream level. Propagation in this manner essentially resets the accumulated deviation from the manifold every $\overline{p}$ iterates; any discontinuities in the extracted arc are

differentially corrected as necessary (and typically in a straightforward computation in this case) [14].

Utilizing the manifold segment tree also simplifies the identification and extraction of free-flowing dynamical connections between orbits. A *heteroclinic* connection (H_c) links a W^U arc originating from one orbit to a W^S arc of another orbit through an intersection point on the Poincaré section (*homoclinic* connections (H_o) bridge W^U to W^S of the *same* orbit) [10].

6 Applications to Astrodynamics

Periodic orbits and associated invariant manifolds supply a rich dynamical knowledge that is essential for a versatile spaceflight design platform. As shown in the following, interactive selection of arcs and design node links broadens the design possibilities with new options and the ability to quickly examine trade-off decisions.

6.1 Analysis of Novel Periodic Orbits

Our method easily locates periodic orbits that are found through conventional analysis (*e.g.*, members of the Lyapunov and resonant orbit families) but it also reveals many periodic orbits that are either challenging to discover with traditional analysis in general, or previously unknown.

At a Jacobi constant level of $C = 3.2$ in the EM system, the closed L_1 and L_2 gateways prohibit flow between the massive bodies, yet chaos is still present. Our results, displayed in Fig. 7, reveal saddles and centers grouped in island chains and saddle-type fixed points within the limited chaotic regions. The periodic orbits in Fig. 7 are displayed in the xy plane (x-axis in red, y-axis in green). In Fig. 7 and subsequent images, fixed points belonging to the same periodic orbit are marked with the same color. At $C = 3.2$, transversality violations are rare within the analysis domain since the chaos is bounded, and the fixed point extraction is relatively straightforward with little need for cell subdivision.

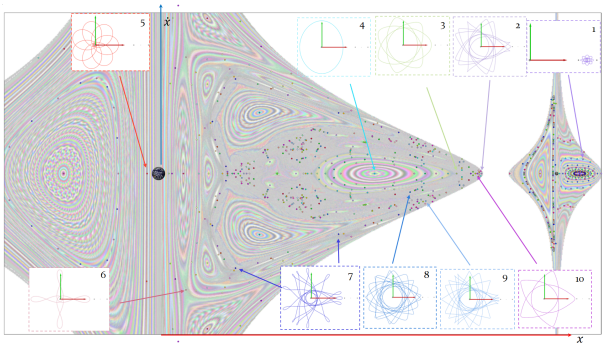

Fig. 7. Fixed points and selected periodic orbits found in the Earth-Moon system at $C = 3.2$.

A more complex yet practically relevant case resides at an energy level where chaos exists throughout the planar flow space. The Earth-Moon system with $C = 2.96$ permits trajectories everywhere in the xy plane. Broader sampling parameters are applied over a larger analysis domain (see Trial 1 in Table 2). We obtain a set of fixed points throughout D_{EM} with sparse behavior capture near lunar vicinity. Therefore, a more refined extraction is performed near the Moon. Refer to Trials 2, 3, and 4 in Table 2. As shown in Fig. 1, the fixed points extracted for $C = 2.96$ in the EM system are numerous, reaching a total of 1450 distinct periodic orbits.

The identified periodic orbits are then inserted in a large database, along with their integral period, stability type, $|\nu_{SI}|$, spatial coordinates as well as overall time period. The corresponding Orbit IDs are listed on the sample orbits shown in Fig. 1 for easy reference during sample design scenarios.

Among the fixed points found at $C = 2.96$, many novel saddle-type periodic orbits were identified. As shown in Fig. 1, several periodic orbits are commonly known such as Orbit 4 (the L_1 Lyapunov), Orbit 23 (1:2 resonant orbit), Orbit 49 (stable 3:2 resonant orbit), Orbit 51 (unstable 3:2 resonant orbit), and Orbit 50 (the $p = 3$ unstable DRO - quasi-periodic island near the Moon) [20, 4, 2]. Several orbits, though, transit between the interior and exterior regions (such as Orbit 1433) and DRO vicinity to exterior or interior (Orbits 229, 826, and 1357). Yet others like Orbit 1439 visit all the aforementioned regions, perhaps making such orbits potentially useful for transfer design. And though the analysis is only performed within the primary analysis domain D_{EM} on the $\Sigma : y = 0$ Poincaré section (as per Table 2) an abundant number of unstable periodic orbits that cross this section travel to L_3, L_4, and L_5 vicinities. Clearly, our results offer a vivid dynamical understanding of this particular system.

Trial	C	Domain $(x, \dot{x})$ (nondim)	Resolution	$l_{\min}$	$p_{\max}$
0	3.2	$[0.4, 1.1] \times [-2.5, 2.5]$	24×16	8×10^{-5}	12
1	2.96	$[0.4, 1.1] \times [-2.5, 2.5]$	24×16	8×10^{-5}	12
2	2.96	$[0.9, 1.0] \times [-1.5, 1.5]$	8×8	2×10^{-5}	12
3	2.96	$[0.78, 0.92] \times [-0.4, 0.4]$	8×8	2×10^{-5}	6
4	2.96	$[0.9925, 1.08] \times [-0.2, 0.2]\}$	6×6	2×10^{-5}	4

Table 2. Parameters used in the Earth-Moon system.

6.2 Poincaré Map Topology Structure

With fixed points extracted, the complete Poincaré map topology structure is characterized by means of our invariant manifold extraction algorithm, which is demonstrated in the Earth-Moon system at $C = 3.2$. The large-scale topology extraction result appears in Fig. 8 with unstable manifolds (W^U) and stable manifolds (W^S) colored in red and blue, respectively. At $C = 3.2$, invariant manifolds are extracted throughout the chaotic areas, thoroughly filling in the phase space areas between quasi-periodic islands. Our algorithm captures saddle-center island chains except on some islands near the Moon. Difficulties near the Moon can be explained by numerical sensitivity and numerical error build-up during integration as trajectories pass exceptionally close to the singularity multiple times before completing the $\overline{p}$-th iterate. As with fixed point extraction, advecting invariant manifolds for the Earth-Moon system at $C = 3.2$ is not as challenging as at other Jacobi constant values since fewer hyperplane transversality violations are encountered. In fact, this manifold set is processed without stability index pre-screening and still completes the advection procedure faster than systems with open gateways. Yet, some challenges in describing the Poincaré map topology skeleton are visible in a close-up representation (Fig. 8(b)). Artifact segments shortcut some tight bends in both manifold types, but these are merely caused by loose curve-refinement parameters. Chaotic tangles, on the other hand, strongly influence the generation of invariant manifolds, especially as a manifold is advected towards the origin fixed point of the opposing stability type.

As evidenced by the tri-lobe structure in Fig. 8(b), it is unclear if the computed structure is a pure saddle-loop (a completely connected tripetal flower) or if the chaotic tangle oscillations in the manifold are the true projection of the invariant manifold streamsurface. Nevertheless, the computed topology skeleton is still an applicable representation of manifold behavior for design practices.

The Poincaré map topology is next extracted on a section with open gateways to permit flow throughout the xy plane. At $C = 2.96$ in the *EM* system, advection produces a depiction of both stable (blue) and unstable (red) manifolds for the periodic orbits shown in Fig. 9. Limits on base orbit stability index ($|\nu_{SI}| \leq 2500$) screen considered fixed points to reduce overall computation during the advection procedure, cutting in half the number of saddle-type orbits included. Even with a selective range on ν_{SI}, the advected set of manifolds populate almost the entire chaotic region. As can be seen , the only areas within the chaotic sea without stable manifolds are associated with trajectories that escape the entire Earth-Moon system. Knowing this highly detailed stable manifold structure, a spacecraft in almost any location within the applicable chaotic sea can reach a stable manifold of some fixed point with a small ΔV . This rich understanding of the available flow is extremely beneficial to spaceflight applications as nearby paths

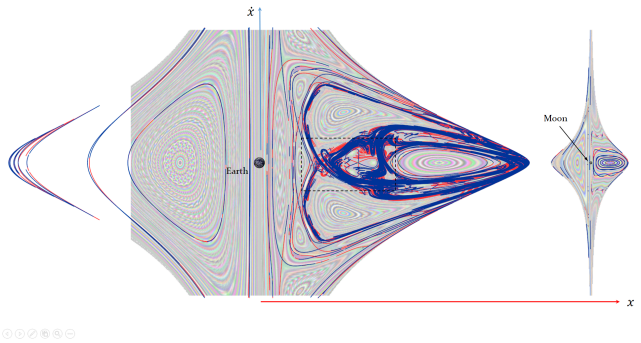

(a) Primary analysis domain D_{EM}

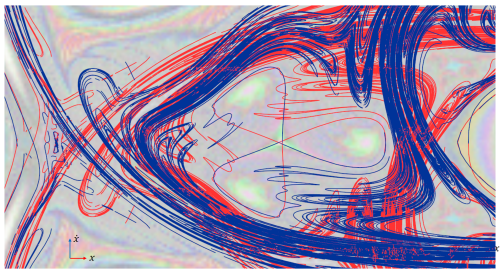

(b) Zoom-in on indicated domain

Fig. 8. The Poincaré map topology skeleton (W^U in red and W^S in blue) computed with the manifold extraction algorithm in the Earth-Moon system within the domain D_{EM} at $C = 3.2$.

to almost any Poincaré section state are revealed.

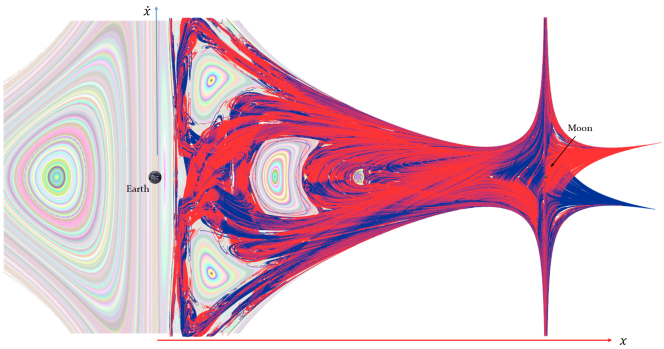

Fig. 9. The Poincaré map topology skeleton (W^U in red and W^S in blue) computed in the Earth-Moon system at $C = 2.96$.

6.3 Design Elements of Poincaré Map Topology in the Earth-Moon System

Manifold arc selection offers a key tool for design construction with Poincaré map topology. Consider the smaller topology skeleton subset that includes just the invariant manifolds of the L_1 Lyapunov and the $p = 3$ unstable DRO, see Fig. 10. The subsample of manifolds appears on the Poincaré section with the W^S and W^U pair colored with black and crimson for the L_1 Lyapunov and with blue and red for the $p = 3$ DRO, respectively. A L_1 Lyapunov stable manifold arc (black) and a $p = 3$ DRO stable manifold arc (blue) are selected at the indicated locations on the Poincaré section (Fig. 10(a)) that originate in the interior region. Both resulting arcs (shown in the rotating frame in Fig. 10(b) and in the inertial frame in Fig. 10(c)) demonstrate an elliptical orbit around the Earth before a second passage where the CR3BP dynamics shift the trajectories towards asymptotic approach of the respective orbits. The time of flight of the transfer trajectory considers the propagation time from the initial selection point until the geometric similarity condition between the manifold and desired orbit [14]. The black arc enters the L_1 Lyapunov orbit at the practical arrival condition after 38.10 days whereas the blue arc practically arrives in the $p = 3$ DRO after 88.14 days. Clearly, the arc selection capability enhances quick design construction by readily incorporating many ballistic capture trajectories.

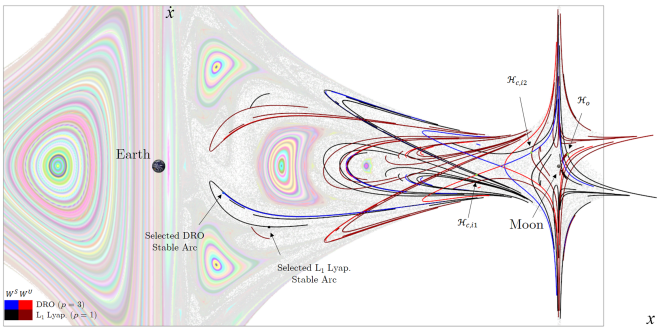

(a) Manifolds of the L_1 Lyapunov and $p = 3$ DRO periodic orbits

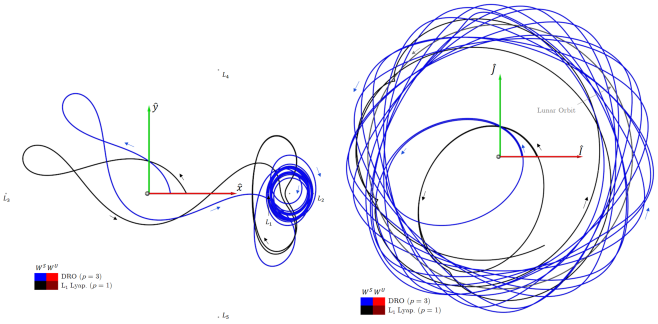

(b) Selected arcs (rotating frame) (c) Selected arcs (inertial frame)

Fig. 10. Invariant manifolds for the L_1 Lyapunov and $p = 3$ DRO saddle-type orbits extracted with PMATE in the Earth-Moon system ($C = 2.96$). Selected stable manifold arcs are displayed in the rotating (b) and inertial (c) frames.

6.4 Sample Connections Between Saddle-type Orbits

Heteroclinic and homoclinic connections between the L_1 Lyapunov orbit and the $p = 3$ DRO are quite simple to extract from Poincaré map topology with manifold selection capabilities. Any intersection of stable and unstable manifolds offers a pathway between their respective fixed point, so a multitude of options exist to exploit natural dynamics to transfer between the two orbits. Also apparent in Fig. 10(a) are green points that signify selected heteroclinic connections between the $p = 3$ DRO and L_1 Lyapunov orbit in the interior region ($H_{c,i1}$ and $H_{c,i2}$). A homoclinic connection for the L_1 Lyapunov orbit also appears in Fig. 10(a) as the point H_o at the intersection of a crimson W^U and a black W^S. The chosen interior connection arcs are displayed in Fig. 11. The simplicity of formulating free-flowing connections between unstable periodic orbits assists designers in evaluating different trade studies to align timing possibilities.

Additional connections are also easy to formulate between a wide variety of periodic orbits. An interesting transfer is demonstrated starting at the $p = 3$ DRO and departing to the rather exotic orbit that visits L_3 and L_4 vicinities while also closely approaching the Moon several times. We refer to this orbit as *Orbit* O^* in the following. The invariant manifold curves of that orbit (displayed in Fig. 12 with indigo and tan colors) indicate that a lot of Poincaré section locations naturally flow

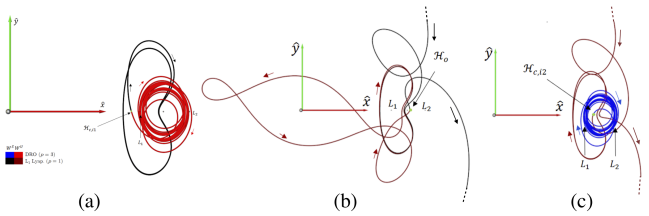

(a) (b) (c)

Fig. 11. Maneuver-free connections between the L_1 Lyapunov orbit and the $p = 3$ DRO constructed through interactive selection of manifold intersection states. (a) $H_{c,i1}$ ($\Delta t = 159.56$ days). (b) $H_{c,i2}$ ($\Delta t = 142.83$ days). (c) L_1 Lyapunov H_o ($\Delta t = 142.99$ days)

into this orbit with the large dispersion of stable manifolds. A transfer from the $p = 3$ DRO to this orbit is represented by any red-indigo intersection, and a selected option demonstrates a transfer possibility as shown in Fig. 12(b). The richness of the available manifold information combined with the the ability to construct heteroclinic connections with ease highlights essential orbits for use as intermediate transfer candidates with a high degree of transfer centrality as indicated through manifold dispersion.

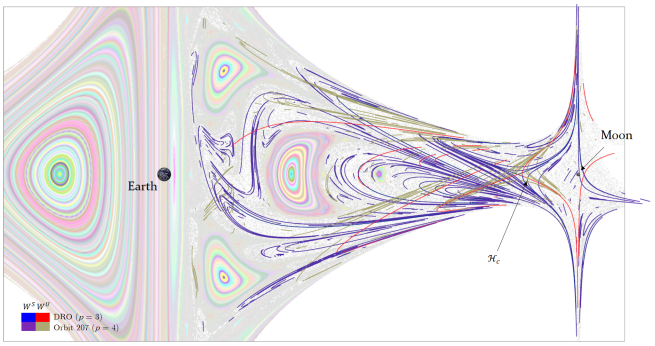

(a) Manifolds for the $p = 3$ DRO and Orbit O^*

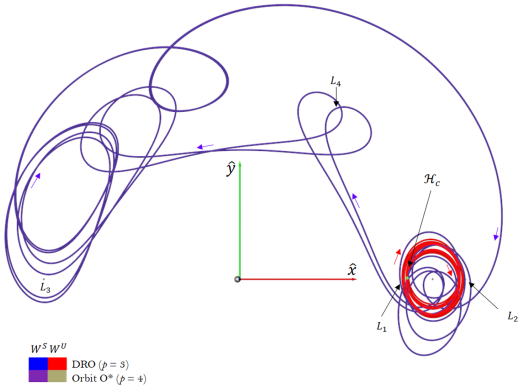

(b) H_c : $p = 3$ DRO to Orbit O^* ($\Delta t = 197.22$ days)

Fig. 12. Invariant manifolds for the $p = 3$ DRO and Orbit O^* extracted with PMATE and a selected heteroclinic connection in the Earth-Moon system ($C = 2.96$).

6.5 Access to Enceladus

A popular topic in astrodynamics research and development is the determination of a low-ΔV pathway to an orbit about Enceladus. A tantalizing prospect for saving ΔV in an Enceladus endgame pathway is the application of a ballistic capture trajectory that exploits stable invariant manifolds, culminating with natural dynamics depositing a spacecraft into a close orbit around Enceladus. The interactive Poincaré map topology design framework (i.e., PMATE and the associated manifold arc extraction) delivers the ability to construct such a ballistic trajectory even without detailed knowledge of the Saturn-Enceladus (*SEnc*) system beforehand.

First, a suitable energy level that permits ballistic capture is sought by utilizing orbit convolution [15] predictions in vicinity of Enceladus. The gravitational influence of Enceladus in the *SEnc* multi-body system is quite diminished versus the lunar influence in the Earth-Moon system (μ_{SEnc} is 5 orders of magnitude smaller than μ_{EM}). Yet, similar multi-body dynamical structure exists in close proximity to Enceladus that can be exploited in a manner analogous to the Earth-Moon system. The $p = 3$ DRO, for example, resides significantly closer to Enceladus in the *SEnc* system versus the similar counterpart in the *EM* system. Utilizing OC imagery, a suitable DRO structure at roughly 600 km is located with $C = 2.999995$ (depicted in Fig. 13(a)) that also possesses safe transfers (not intersecting Enceladus). PMATE is employed to extract fixed points and invariant manifolds throughout the *SEnc* system (refer to Schlei[14] for parameter specifications). As shown by the Poincaré section depictions in Fig. 13(a), the unstable $p = 3$ DRO stable manifold subspace (light blue segments) demonstrates many selectable asymptotic approach arcs without Enceladus intersections, originating near Enceladus and around the L_3 area (Fig. 13(b)). Also, multiple transfer options are available as indicated by the numerous intersections between the $p = 3$ DRO stable manifold and various unstable manifolds of other orbits (red in Fig. 13(a)).

A particular pathway for potential ballistic capture about Enceladus is easily chosen incorporating manifold arc reconstruction within the L_3 vicinity (Fig. 13(b)). Note, the red and blue manifolds of Fig. 13(a) permeate the chaotic regions in the L_3 vicinity as well but are removed from the representation in Fig. 13(b) for clarity. A particular location along the $p = 3$ DRO stable manifold is selected interactively to produce the trajectory represented in Fig. 13(c). This selected W^S arc performs one and a half revolutions around Saturn before one of the inward reaching loops lines up with an Enceladus close passage to then asymptotically approach the $p = 3$ DRO. Many additional locations within the indicated zone in Fig. 13(b) highlight where ballistic capture about Enceladus is also possible. From a spacecraft path-planning standpoint, the solutions from PMATE characterize the *SEnc* system flow and provide endgame target solutions[14].

6.6 Rerouting Scenario

A scenario where an adaptation to a spacecraft destination is sought illustrates the application of extracted Poincaré map topology to a versatile design paradigm. Assume that a spacecraft with a small amount of remaining fuel is on an undesirable trajectory leaving the Earth-Moon system, creating a desire to reroute the spacecraft to a new destination. Such a scenario is indicative of either a cube satellite that is dropped off from a larger spacecraft or a vehicle at the end of a primary mission. The current Poincaré map state of the undesired effect is $(x, \dot{x}) = (0.8455137, -0.1859837)$ in nondimensional rotating frame coordinates on $\Sigma : y = 0$ at $C = 2.96$ (chosen arbitrarily). The future path, displayed as the red arc in Fig. 14, performs a pair of lunar flybys before departing Earth-Moon vicinity. In this scenario, the primary mission constraint is to simply avert the spacecraft from escaping Earth-Moon vicinity subject to available spacecraft resources, namely a ΔV budget arbitrarily set at $\Delta V \leq 20$ m/s.

The rerouting maneuver is designed by examining the nearby stable manifolds on the Poincaré section resulting from PMATE trials (mainly the stable manifolds from Fig. 9). The maneuver budget constraint is portrayed visually as a green bounding box surrounding the current map state (red) on the Poincaré section in Fig. 14. Translation on the Poincaré section is possible via a maneuver that preserves the C-value, constraining movement to the vertical maneuver line. The W^S collection from Fig. 9 is also added to locate flow reachable from the current state. Each stable manifold projection is displayed with a unique bluish hue to signify different base orbits. The wealth of nearby stable manifold structure permits a redirection of the spacecraft to a new destination. With our technique, a user quickly examines multiple

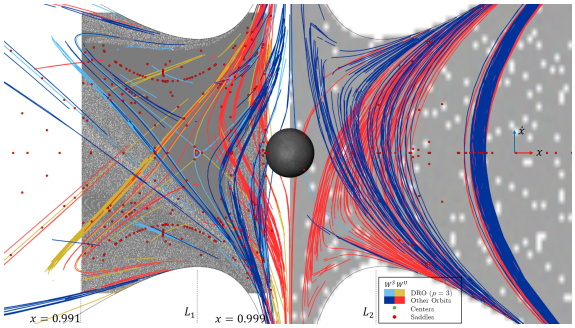

(a) Poincaré section in Enceladus area

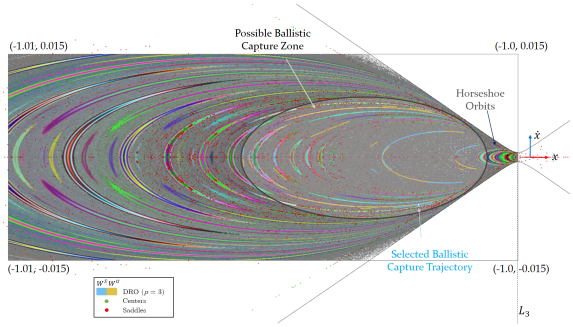

(b) Poincaré section near L_3

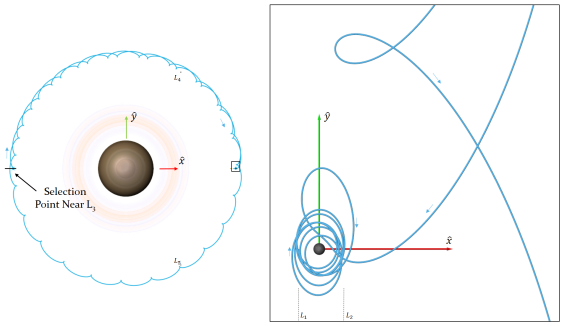

(c) Selected capture arc ($p = 3$ DRO W^S)

Fig. 13. A plausible region for ballistic capture about Enceladus indicated on a Poincaré section with a selected example $p = 3$ DRO manifold arc in the *SEnc* system at $C = 2.999995$.

design options by hovering the mouse over various stable manifolds to observe potential new destination orbits and the ΔV requirements[14]. Fig. 14 also displays some selected stable manifold arcs within the limited resource budget with the necessary ΔV (and $\Delta\dot{x}$ in brackets). Stable manifold arcs that impact the Moon are indicated by the gray bands, but several impact-safe structures exist within reach of the current state. Possible new destinations include Orbits 71 and 331 visiting the interior region. Exterior region options are also available with Orbits 25, 72, 74, and 383. The spacecraft could even potentially depart towards L_4 or L_5 structures with Orbits 16 and 206, respectively, with still over half of the resources available for additional maneuvers later. More destinations are also possible even within this small region as only invariant manifolds of periodic orbits that possess $|\nu_{SI}| \leq 2500$ are depicted. As demonstrated here, thorough knowledge of the stable manifolds enables the quick correction of a deviation from an intended path or the adaptation of the design to a new destination.

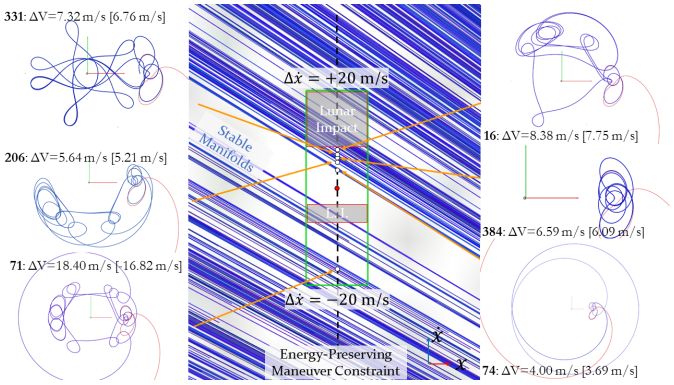

Fig. 14. A Poincaré section displaying a current trajectory map state (red dot producing the red arc) and possible nearby stable invariant manifolds that are reachable with a $\Delta V \leq 20$ m/s (indicated with green bounding box) employing a map-preserving maneuver in the Earth-Moon system ($C = 2.96$).

7 Conclusion

We have presented a computational framework for the visual analysis of the Poincaré map topology in the circular restricted three body problem to assist space trajectory design. In particular, we have described various algorithmic solutions that together enable the automatic extraction of the topology in the CR3BP, specifically periodic orbits and associated invariant manifolds. In this context, we have discussed the challenges that are specific to this type of system and proposed a range of improvements over existing methods to address them.

As we have shown, our method exposes the connectivity of orbital structures, which offers spacecraft trajectory designer a broad range of interactive options without external computation. Our experimentation with this approach suggests that a designer could employ automated topological skeletons as an input catalog to select pathways that navigate the available dynamical flow. By selecting stable and unstable manifolds of various fixed points that are available on a Poincaré map, low-cost transfers are simply traced through the stable-unstable manifold network since all of the relevant orbital data is automatically generated as part of the process. With our proposed manifold construction, linear intersections tests for the numerous segments of the manifolds can autonomously deliver cost-free connections between periodic orbits for additional design options during path planning. In the future, a logical step towards limiting computation exists, namely finding periodic orbits that are central to the problem, driving the underlying topology. Restricting the visual analysis to just those central orbits could greatly reduce the computational effort, but a function to determine orbit centrality is still an open problem.

References

[1] S. Campagnola and R. P. Russell. Endgame problem part 1: v_∞-leveraging technique and the leveraging graph. *Journal of Guidance, Control, and Dynamics*, 33(2):463–475, 2010.

[2] L. Capdevila. A Transfer Network Linking Earth, Moon, and the Triangular Libration Point Regions in the Earth-Moon System. Ph.D. Dissertation, School of Aeronautics and Astronautics, Purdue University, West Lafayette, Indiana, 2016.

[3] J. M. Danby. *Fundamentals of Celestial Mechanics*. Willmann-Bell, Inc., Richmond, Virginia, 2nd edition, 1992.

[4] J. Demeyer and P. Gurfil. Transfer to Distant Retrograde Orbits Using Manifold Theory. *Journal of Guidance, Control, and Dynamics*, 30(5), 2007.

[5] J. England, B. Krauskopf, and H. Osinga. Computing One-Dimensional Global Manifolds of Poincaré Maps by Continuation. *SIAM Journal of Applied Dynamical Systems*, 4(4):1008–1041, 2005.

[6] J. S. Eterno. Attitude Determination and Control. In W. J. Larson and J. R. Wertz, editors, *Space Mission Analysis and Design*, pages 354–380. Microcosm Press, El Segundo, California, 1999.

[7] J. Guckenheimer and P. Holmes. *Nonlinear Oscillations, Dynamical Systems, and Bifurcations of Vector Fields*. Springer-Verlag, New York, 1983.

[8] A. Haapala and K. C. Howell. Trajectory Design Strategies Applied to Temporary Comet Capture Including Poincaré Maps and Invariant Manifolds. *Celestial Mechanics and Dynamical Astronomy*, 116(3):299–323, July 2013.

[9] W. S. Koon, M. W. Lo, J. E. Marsden, and S. D. Ross. Heteroclinic Connections between Periodic Orbits and Resonance Transitions in Celestial Mechanics. *Chaos*, 10(2):427–469, 2000.

[10] A. J. Lichtenberg and M. A. Lieberman. *Regular and Chaotic Dynamics*. Springer-Verlag, New York, New York, 2nd edition, 1992.

[11] M. W. Lo, R. L. Anderson, G. Whiffen, and L. Romans. The Role of Invariant Manifolds in Low Thrust Trajectory Design (Part I). In *AAS/AIAA Spaceflight Dynamics Conference*, Maui, Hawaii, February 2004. Paper AAS 04-288.

[12] W. H. Press, S. A. Teukolsky, W. T. Vetterling, and B. P. Flannery. *Numerical Recipes: The Art of Scientific Computing*. Cambridge University Press, New York, 3rd edition, 2007.

[13] S. D. Ross, W. S. Koon, M. W. Lo, and J. E. Marsden. Design of a multi-moon orbiter. In *AAS/AIAA Space Flight Mechanics Meeting*, Ponce, Puerto Rico, February 2003. Paper AAS03-143.

[14] W. Schlei. Interactive Spacecraft Trajectory Design Strategies Featuring Poincaré Map Topology. Ph.D. Dissertation, School of Aeronautics and Astronautics, Purdue University, West Lafayette, Indiana, 2017.

[15] W. Schlei, K. C. Howell, X. Tricoche, and C. Garth. Enhanced visualization and autonomous extraction of poincaré map topology. *The Journal of the Astronautical Sciences*, pages 1–28, 2015.

[16] J. A. Sims, J. M. Longuski, and A. Staugler. V-infinity Leveraging for Interplanetary Missions: Multiple-RevolutionOrbit Techniques. *Journal of Guidance, Control and Dynamics*, 20(3):409–415, 1994.

[17] N. J. Strange, S. Campagnola, and R. P. Russell. Leveraging flybys of low mass moons to enable an enceladus orbiter. *Advances in the Astronautical Sciences*, 135(3):2207–2225, 2009.

[18] S. H. Strogatz. *Nonlinear Dynamics and Chaos*. Westview Press, Perseus Books Publishing, Cambridge, Massachusetts, 1994.

[19] V. Szebehely and H. Mark. *Adventures in Celestial Mechanics*. John Wiley and Sons, Inc., New York, New York, 2nd edition, 1998.

[20] T. M. Vaquero Escribano. Poincaré Sections and Resonant Orbits in the Restricted Three-Body Problem. M.S. Thesis, School of Aeronautics and Astronautics, Purdue University, West Lafayette, Indiana, 2010.

[21] X. Tricoche, C. Garth, and A. Sanderson. Visualization of Topological Structures in Area-Preserving Maps. *IEEE Transactions on Visualization and Computer Graphics*, 17(12):1765–1774, 2011.

[22] M. Vaquero and K. C. Howell. Transfer Design Exploiting Resonant Orbits and Manifolds in the Saturn-Titan System. *Journal of Spacecraft and Rockets*, 50(5):1069–1085, February 2013.

[23] J. R. Wertz. Space Mission Geometry. In W. J. Larson and J. R. Wertz, editors, *Space Mission Analysis and Design*, pages 95–130. Microcosm Press, El Segundo, California, 1999.

[24] J. R. Wertz, R. C. Conger, M. Rufer, N. Sarzi-Amade, and R. E. V. Allen. Methods for Achieving Dramatic Reductions in Space Mission Cost. In *Reinventing Space Conference*, Los Angeles, California, March 2011.

[25] S. N. Williams. Automated Design of Multiple Encounter Gravity-Assist Trajectories. M.S. Thesis, School of Aeronautics and Astronautics, Purdue University, West Lafayette, Indiana, 1990.

[26] J. R. Yim, J. L. Crassidis, and J. L. Junkins. Autonomous orbit navigation of interplanetary spacecraft. In *AIAA/AAS Astrodynamics Specialist Conference*, Denver, Colorado, August 2000. Paper AIAA 2000-3936.